Available online at www.sciencedirect.com

Journal of the European Ceramic Society 30 (2010) 669–675

www.elsevier.com/locate/jeurceramsoc

Microstructures and mechanical properties of $Ce_{1-x}Ca_xO_{2-y}$ ($x = 0.05, 0.1, 0.2$) with different sintering temperatures

M. Yan[a,*], T. Mori[a], J. Zou[b,c], H. Huang[b], J. Drennan[c]

[a] Fuel Cell Materials Center, National Institute for Materials Science, 1-1 Namiki, Tsukuba, Ibaraki 305-0044, Japan
[b] School of Mechanical and Mining Engineering, The University of Queensland, Brisbane, QLD 4072, Australia
[c] Centre for Microscopy and Microanalysis, The University of Queensland, Brisbane, QLD 4072, Australia

Received 20 February 2009; received in revised form 13 August 2009; accepted 7 September 2009
Available online 26 September 2009

Abstract

In this study, the microstructures and mechanical properties of Ca-doped CeO_2 affected by different sintering temperatures and various dopant concentrations have been systematically investigated. Transmission electron microscopy (TEM) and X-ray diffraction (XRD) revealed that a seemingly individual Ca-doped CeO_2 system may consist of multiple types of doped CeO_2 phases. X-ray photoelectron spectroscopy (XPS) analysis demonstrated that the chemical state of the Ce element is less dependent on the sintering temperature, while increasing the sintering temperature may cause segregation of the Ca elements to form CaO phase. Nanoindentation tests showed that Ca-doped CeO_2 has better fracture toughness compared to rare-earth (RE) doped CeO_2; the relationship between the sintering temperature and the mechanical property has been discussed.

Keywords: Microstructure-final; Mechanical properties; Fuel cells; Sintering

1. Introduction

Solid oxide fuel cells (SOFCs) can provide clean and efficient energy for a variety of applications, ranging from small portable power units to large scale electricity plants.[1–5] A successful fabrication of an SOFC demands a highly conductive and mechanically stable electrolyte, which is the key part of an SOFC assembly. In this aspect, doped CeO_2 is one of the strong candidates, and considerable attention has been drawn on its developing in recent years.[6–8]

Although RE-doped CeO_2 shows good ionic conductivity at the intermediate temperature region, by comparison, Ca-doped CeO_2 has demonstrated two major superiorities: (1) a less environmental burden and (2) a lower production cost, both of which are essential for the industrialization of SOFCs in the current environment.[9,10] It is noticed that, however, the microstructural characteristics of Ca-doped CeO_2 with different doping levels and various sintering temperatures are poorly understood, although such knowledge is vital for the practical design and application of electrolytes. In particular, extensive studies on RE-doped CeO_2 have shown that fine microstructures and microstructural variations (as a function of doping level and sintering temperature) play a key role in their conductivities.[11–13] On the other hand, mechanical properties of electrolytes are also important when considering the necessarily long term service of SOFCs, which is susceptible to thermal stress and mechanical stress during the cell operation. Because of this, various mechanical properties have been investigated for RE-doped CeO_2, such as elastic modulus,[14,15] hardness,[16,17] and fracture toughness.[14,16–19] In contrast, relevant study can be barely found for Ca-doped CeO_2.

For the aforementioned reasons, in the current study, microstructure and mechanical properties of $Ce_{1-x}Ca_xO_{2-y}$ ($x = 0.05, 0.1, 0.2$) with various doping levels and different sintering temperatures have been systematically investigated. This Ca-doped CeO_2, when developed properly, has shown competitive conductivity compared to RE-doped CeO_2.[20] In the meanwhile, its ionic transference number, although not studied, should be high enough in a wide oxygen partial pressure region

---

[*] Corresponding author. Present address: School of Mechanical and Mining Engineering, The University of Queensland, Cooper Road, Brisbane, QLD 4072, Australia.

E-mail address: m.yan2@uq.edu.au (M. Yan).

0955-2219/$ – see front matter © 2009 Elsevier Ltd. All rights reserved.
doi:10.1016/j.jeurceramsoc.2009.09.005

according to the literature on RE-doped CeO_2.[21] All of these suggest that it is a promising electrolyte material for SOFCs and also justify this research.

2. Materials and methods

2.1. Materials

The powder-form precursors of $Ce_{1-x}Ca_xO_{2-y}$ ($x = 0.05$, 0.1 and 0.2) were prepared using a co-precipitation method.[22] The powders were firstly calcined at 700 °C for 2 h and then compacted into pellets under a rubber press of ~15 MPa. The compacted pellets were subsequently sintered at five different temperatures, i.e., 1100 °C, 1150 °C, 1200 °C, 1250 °C and 1300 °C, for 4 h. Accordingly, in total, 15 types of sintered pellets were investigated. To simplify, we will use a shortened form to express the sample state hereafter. For example, 5Ca-1100 refers to the sample of $Ce_{0.95}Ca_{0.05}O_{2-y}$ sintered at 1100 °C.

The densities of the sintered pellets were measured using the Archimedes method and all the densities were found to be ~95% of the respective theoretical density. The average grain size was determined by counting over 500 grains for each specimen via scanning electron microscopy (SEM) observations. Polished specimens were used in the mechanical property tests.

2.2. Microstructure analyses

TEM was performed on a JEOL NM-200 (operated at 200 kV). Scanning electron microscopy (SEM, Hitachi S-5000, operated at 20 KV) and XRD (Rigaku RINT 2000HF Ultima, Cu Kα, 40 kV/40 mA) were also used for the microstructure analysis. XPS was conducted on a PHI 5700 ESCA system in a chamber pressure of $(5–8) \times 10^{-9}$ Torr. Argon ions were used to sputter off layers from sample to investigate the XPS responses from various sample depths. A monochromatic Al Kα X-ray (1486.6 eV) was used as the incident radiation. The XPS spectrum was recorded at a constant analyzer with a pass energy of 187.85 eV, and the high resolution analysis was conducted at a pass energy of 29.35 eV. The softwares (PC-ACCESS and Peakfit V4.12) were used to analyze the recorded XPS spectra and XRD patterns, respectively.

2.3. Mechanical property tests

Nanoindentation tests (samples ~Ø3 mm × 2 mm) were carried out on a HYSITRON TriboIndenter® nanomechanical testing instrument at room temperature in ambient environment. A three-sided Berkovich indenter with an included angle of 142.3° and a tip radius of 100 nm was used. For each specimen, a number of indents were made at different loads ranging from 1000 to 6000 μN. In each indentation, the indenter was linearly loaded to the preset maximum value within 5 s, held at the maximum load for 10 s, and then unloaded linearly within 10 s. The reduced modulus, E_r, of the tested specimen was determined using the slope of the unloading segment of the load–displacement curve.[23] The elastic modulus of the specimen, E_s, was thus calculated using the following equation[23]:

$$\frac{1}{E_r} = \frac{1 - V_i^2}{E_i} + \frac{1 - V_s^2}{E_s} \tag{1}$$

where $E_i = 1141$ GPa and $V_i = 0.07$ were the elastic modulus and Poisson's ratio of the diamond indenter, respectively. The Poisson's ratio of the specimen, V_s, used in this study was assumed to be 0.3.[15]

Vickers hardness tests (samples ~Ø10 × 3 mm) were carried out on an HBV-30A Briviskop using a pyramid indenter at the room temperature. For each test, a load range of 2000–3000 gf was used and the holding time was ~20 s at the maximum load; at least three indents were made for each specimen.[24] Vickers hardness, H_v (in GPa), of the tested specimen was determined using the following equation:

$$H_v = \frac{0.018F}{d^2} \tag{2}$$

where F was the load in the unit of kgf and d was the average value of the diagonal lengths.

Based on the elastic modulus (E) obtained from the nanoindentation test and the Vickers hardness (H_v), the fracture toughness (K_{IC}) can be estimated using the equation shown below[25]:

$$K_{IC} = 0.016\left(\frac{E}{H_v}\right)^{1/2} \frac{P}{C^{3/2}} \tag{3}$$

where P was the load used in the Vickers hardness test and C was the average radical crack length measured using SEM.

3. Results and discussion

3.1. XRD and TEM characterization

Fig. 1 presents the representative XRD patterns for Ca-doped CeO_2 with different dopant concentrations and sintering temperatures, suggesting that the face centered cubic (FCC) structured doped CeO_2 phase is dominant in these statuses; the crystal structure of doped CeO_2 is confirmed by the selected area electron diffraction (SAED) patterns along the zone axes of [1 1 0], [1 0 0] and [5 1 0] (refer to the inset in Fig. 1). It is noticed that no evident microstructural variations are observable within these differently sintered specimens. Traces of the secondary phase, however, are detectable in the case of the 20Ca doping (e.g., the small diffraction peak at the 2θ of 37°), whose crystal structure was determined as an FCC with a ~0.48 nm (identical to the CaO phase) by our previous study.[26] In the meanwhile, it is found that the XRD evidence of the secondary phase is barely observable in the dopant concentrations of 5Ca and 10Ca.

According to the XRD results, it seems that a monolithic doped CeO_2 phase dominates the specimens. However, careful analysis of the XRD patterns suggests that extra structural features exist as well. As shown in Fig. 2, the deconvolution results of the XRD patterns are realized within the 2θ angles from 78° to 81° for several representative samples, with increasing the dopant concentration from 5Ca to 20Ca [Fig. 2(a)–(c)] and

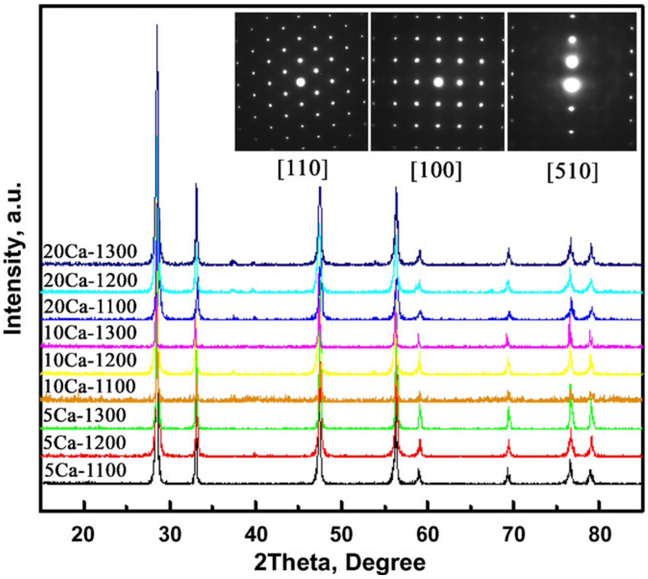

Fig. 1. Representative XPD patterns for 5Ca, 10Ca and 20Ca-doped CeO_2. Inset showing in-zone TEM-SAED patterns for the FCC structured doped CeO_2 phase.

increasing the sintering temperature from 1100 °C to 1300 °C [Fig. 2(b), (d) and (e)]. As shown in Fig. 2(a), it is interesting to note that two or even more components rather than one can be deconvoluted, which are also observable in Fig. 2 (b) and (c). Judging by the peak positions, it is noticed that these two components (for instance) are different from the one that responsible for the (4 0 0) plane of the CaO phase as shown in Fig. 2(b) and (c), suggesting that they are not contributed from CaO phase. In consequence, they should be resulted from the Ca-doped CeO_2, suggesting at least two types of Ca-doped CeO_2 phases exist and they are responsible for the appearance of these XRD signals. A highly possible reason for this multiple-phase coexisting phenomenon could be the different amounts of Ca in these Ca-doped CeO_2 phases, leading to various lattice parameters which are close to each other and hardly perceptible in the low angle XRD diffraction patterns. In fact, Ca-doped CeO_2 does show lattice variations from ~0.5407 nm to ~0.5417 nm when the doping level increases from 0% to 20%.[27–29] In comparison, even higher degree of lattice variation can be encountered in RE-doped CeO_2, e.g., from ~(0.5407–0.5411) nm to ~(0.5432–0.5440) nm for Sm-doped CeO_2.[29,30] Accordingly, it is very possible that this multiple-phase coexisting is also realizable in the RE-doped CeO_2 materials.

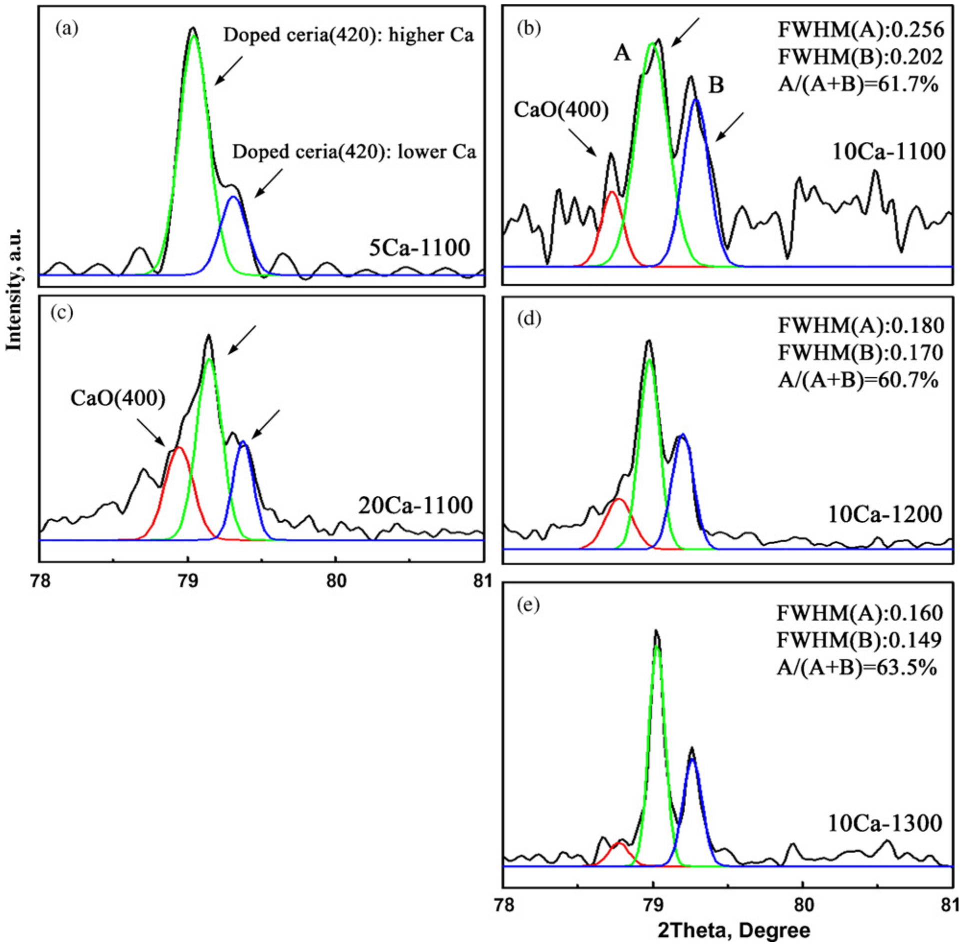

Fig. 2. Deconvolution results for XRD patterns of: (a) 5Ca-1100, (b) 10Ca-1100, (c) 20Ca-1100, (d) 10Ca-1200 and (e) 10Ca-1300. Characters of (A) and (B) denote the area fraction of the high Ca-containing and low Ca-containing doped CeO_2 phases. Error limits are estimated to be within ±5%.

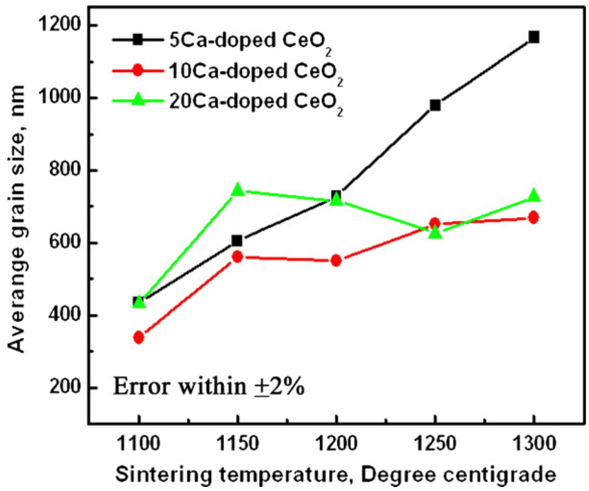

Fig. 3. Average grain size of the sintered pellets as a function of the sintering temperature.

Moreover, by comparing Fig. 2(b), (d) and (e) that for 10Ca-doped CeO$_2$ with the increasing sintering temperatures, three characteristics can be noticed: (1) by a rough estimation, the area fraction of the CaO (4 0 0) signal in the total XRD signal decreases, suggesting that higher sintering temperature can enhance the solution of the Ca element. It should be mentioned that, in fact, the XRD signals for the CaO phase are rather weak in this dopant concentration and they are usually entangled with the background, making a quantitative evaluation of their area fraction unavailable; (2) the area fractions of the high Ca-containing CeO$_2$ (peak A, corresponding to a larger lattice parameter) and low Ca-containing CeO$_2$ (peak B, corresponding to a smaller lattice parameter) remain stable (vibrating around 60%), suggesting that the sintering temperature has less effects on the redistribution of the Ca element; (3) the full-width-half-maximum (FWHM) values of the main peaks (refer to A and B that for the doped CeO$_2$ phases) decrease, suggesting enlarged grain size with the increasing sintering temperatures according to the well-known Scherrer equation that regulates the relationship between the grain size and the FWHM value [$d = 0.89\lambda/(B\cos\theta)$, where λ is the x-ray wavelength, d is the grain size and B is the FWHM value]. The measured average grain size via SEM observation in Fig. 3 confirms this point, showing a generally increased grain size with the increasing sintering temperature, while there is no constant tendency observable among different dopant concentrations.

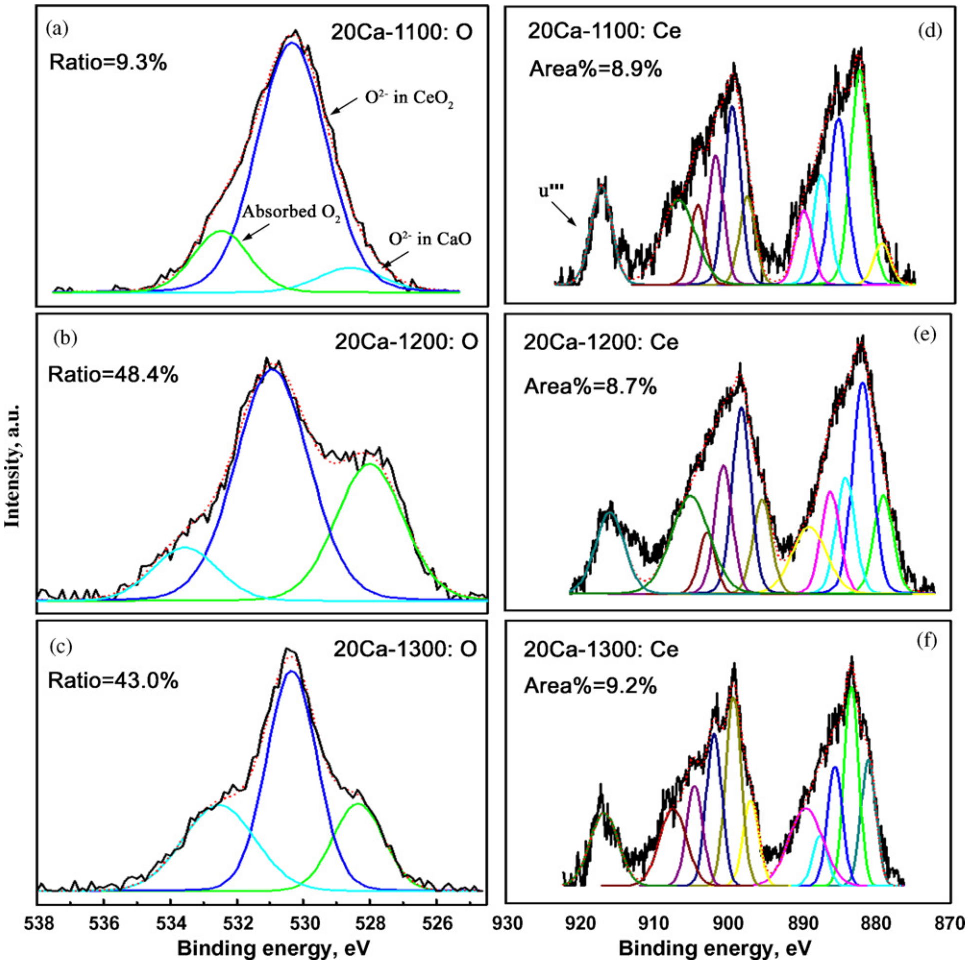

Fig. 4. XPS spectra showing the sintering temperature effects on the XPS responses of the 20Ca samples: (a–c) for the O 1s signals and (d–f) for the Ce 3d signals. The signal was acquired from the layer of ~5 nm below the raw surface. Error limits are estimated to be within ±5%.

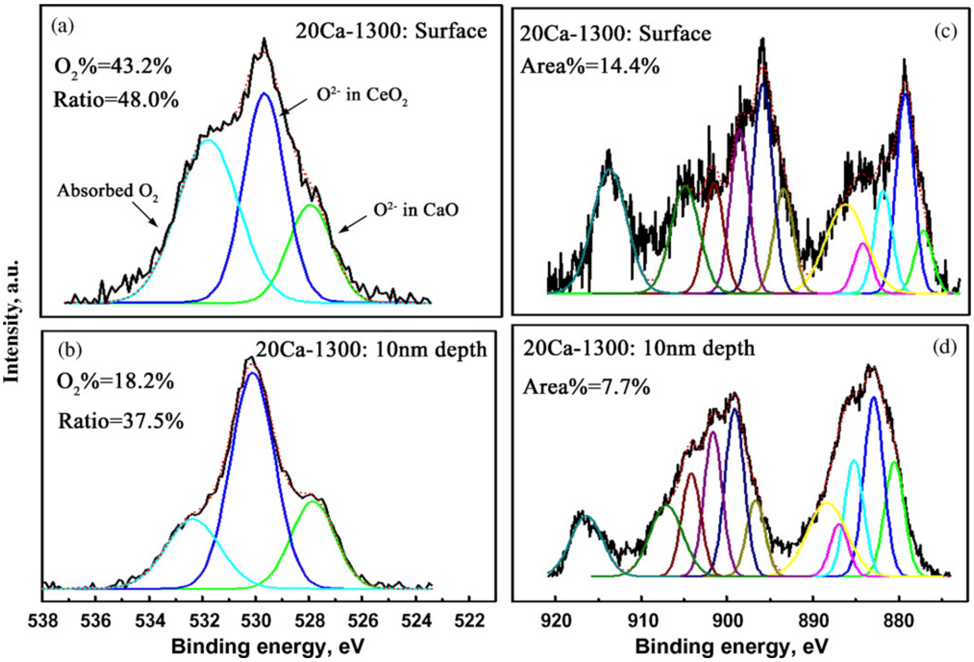

Fig. 5. XPS spectra showing the depth effects on the XPS response from the example of 20Ca-1300: (a and b) for the O 1s signals and (c and d) for the Ce 3d signals. Error limits are estimated to be within ±5%.

3.2. XPS analysis

In our previous study, it has been quantitatively elucidated that increasing the dopant concentration will lead to a reduction of Ce from Ce^{4+} state towards a combination of $(Ce^{3+} + Ce^{4+})$.[26] In this study, the focus will be on the XPS responses that affected by the various sintering temperatures. Fig. 4 presents the XPS spectra with Fig. 4(a)–(c) for O 1s and Fig. 4(d)–(f) for Ce 3d (collected from 20Ca that sintered at increasing temperatures as the typical examples, analysis layer ~5 nm below raw surface). It should be mentioned that CaO exists at this dopant concentration as a secondary phase. In subsequence, the O 1s spectrum can be deconvoluted by three components as illustrated by Fig. 4(a), arising from the absorbed oxygen,[31] O^{2-} in the doped ceria phase(s)[13] [shortened as $O^{2-}|CeO_2$] and O^{2-} in CaO phase [shortened as $O^{2-}|CaO$].[26] The ratio of area fraction between $O^{2-}|CaO$ and $O^{2-}|CeO_2$ is also listed in Fig. 4(a)–(c). Accordingly, it can be noted that increasing the sintering temperature can significantly enlarge the area fraction of $O^{2-}|CaO$ from 9.3% to over 40.0%, suggesting that a segregation of the Ca element (from the Ca-doped CeO_2 towards the CaO phase) will be encouraged by the high temperature sintering. On the other hand, since it is generally believed that the u''' peak of the Ce 3d spectrum can qualitatively reveal the reduction degree of CeO_2 or doped CeO_2 materials,[32] the area fraction of this peak was calculated and the results are shown in Fig. 4(d)–(f). Taking the measurement errors into account, no obvious difference can be found for these Ca-doped CeO_2 that sintered at increasing temperatures, suggesting that the reduction is less dependent upon the sintering temperature than the dopant concentration as we determined previously.[26]

By combining the XRD and TEM results with the XPS analysis, the following can be realized for the differently sintered Ca-doped CeO_2: by increasing the sintering temperature, the solution of CaO increases as a whole (based on the XRD analysis); at the same time, the tendency of CaO phase's segregation increases. The latter, however, may only happen in the surface or near-surface layers. In this aspect, Fig. 5 provides a detailed illustration based on the O 1s spectra and Ce 3d spectra from different sample layers, i.e., the original surface and the layer ~10 nm below the original surface, respectively. The amount of the absorbed oxygen (O_2%), the ratio (Ratio) between $O^{2-}|CaO$ and $O^{2-}|CeO_2$ and the area fraction of the u''' peak in the total Ce 3d signal (Area%) are listed in these figures. Based on this, it can be found that: (1) the ratio between $O^{2-}|CaO$ and $O^{2-}|CeO_2$ decreases with the depth, suggesting that the Ca element tends to aggregate in the outside layers; (2) the original surface corresponds to a higher Ce^{4+} concentration when compared to the depth of ~10 nm; (3) the original surface contains a higher amount of absorbed oxygen, showing a decrease from ~43.2% at the original surface to ~18.2% that for the ~10 nm depth. This also explains the higher Ce^{4+} concentration in the original surface that benefited from a relatively oxygen-sufficient atmosphere.[33]

3.3. Mechanical properties

Fig. 6 shows the Vickers hardness of 5Ca-, 10Ca- and 20Ca-doped CeO_2 as a function of the sintering temperature. Based on this, it can be seen that the hardness is significantly affected by the sintering temperature, with an increase in the sintering temperature generally resulting in a decrease in the hardness for all the three dopant concentrations. In the meanwhile, the effect of the dopant concentration on the hardness is less evident. Moreover, as shown in Fig. 3 that the grain size increases with the increasing sintering temperature, the effect of the sintering

Table 1
Mechanical properties of doped CeO_2 materials. Elastic modulus (GPa), fracture toughness ($MPa\,m^{1/2}$) and hardness (GPa) values are listed based on the current study and the references.[14–19] The properties for Ca-doped CeO_2 vary with different sintering temperatures; Gd- and Sm-doped CeO_2 also vary in properties among different references.

Dopant concentration	Ca			Gd			Sm		
	E	K_{IC}	H_v	E	K_{IC}	H_v	E	K_{IC}	H_v
5 at.%	205–256.5	2.27–3.42	6.22–9.26	170	1.3	–	170	1.3	–
10 at.%	254	2.45	6.84–8.13	160 or 254.6	1.3 or 2.08	–	150	1.3 or 2.4	–
20 at.%	239	2.19	7.24–8.74	125	1 or 1.47	9.25	100	0.85 or 2.3 or 2.4	8.2

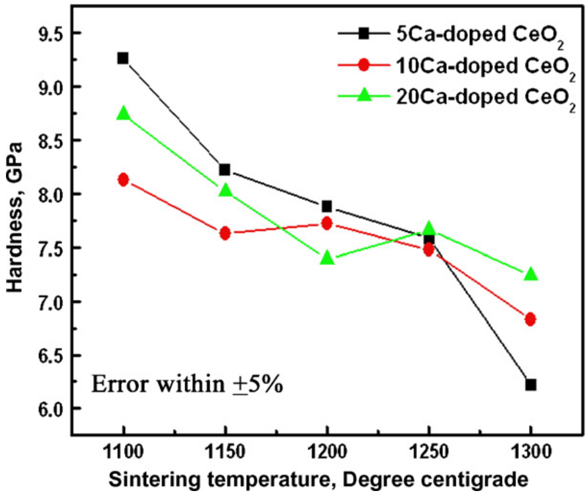

Fig. 6. Vickers hardness of Ca-doped CeO_2 as a function of the sintering temperature.

temperature on the hardness thus can be generally explained by the well-known Hall–Petch relationship ($H = H_0 + kd^{-1/2}$, where H is the hardness, H_0 is a constant and d is the diameter of grain).

To specify the elastic modulus, nanoindentation was performed and the relevant results are shown in Fig. 7. Fig. 7(a) is a typical load–displacement curve obtained from the indentation on 20Ca-1150. A small "pop-in" is observable at approximately 2500 μN in the loading process. This "pop-in" is very likely resulted from a microfracture event associating with the loading process, indicating that the material is brittle. Inset in Fig. 7(a) is an in situ AFM image of the indent made at ∼5000 μN. The impression appears to be well formed and no apparent pile-up or sink-in can be observed.

Based on the load–displacement curves recorded from the nanoindentation tests, the elastic moduli of the specimens were determined and the results are plotted in Fig. 7(b) and (c) as functions of the sintering temperature and the dopant concentration, respectively. Based on these, it is apparent that the average elastic modulus demonstrates a tendency of slight decrease with increasing the sintering temperature [Fig. 7(b)] or dopant concentration [Fig. 7(c)]. Previous studies have shown that the lattice spacing of doped CeO_2 materials increases when increasing sintering temperature or dopant concentration.[34,35] Consequently, the enlarged lattice spacing, which usually leads to an enlarged atomic distance then affects the modulus negatively, could be the reason for the observed decreased modulus. It is also noted that the elastic moduli obtained from the nanoindentation tests are scattering to some extent, which might be affected by the different amounts of weak grain boundaries covered by each nanoindentation test.

In order to compare the mechanical properties of Ca-doped CeO_2 with RE-doped CeO_2, the values of elastic modulus, fracture toughness and hardness obtained from the current study are listed in Table 1, together with those for Gd- and Sm-doped CeO_2 as representatives for RE-doped CeO_2.

In terms of the elastic modulus, one may notice that the value for Ca-doped CeO_2 is higher than those for the Sm-doped CeO_2 and Gd-doped CeO_2 in the case of 5% element doping; it is close to the Gd-doped CeO_2 when the doping amount is 10%.[14–19] Based on the available lattice parameters for Ca-, Gd-, and Sm-doped CeO_2, 10% dopant for instance, Ca-doped CeO_2 shows a lattice parameter (∼0.5415 nm) similar to Gd-doped CeO_2 (∼0.5415 nm) but smaller than Sm-doped CeO_2 (∼0.5420 nm),[27–30,36] which may favorably affect the elastic modulus. Combined with moderate hardness, as listed in the

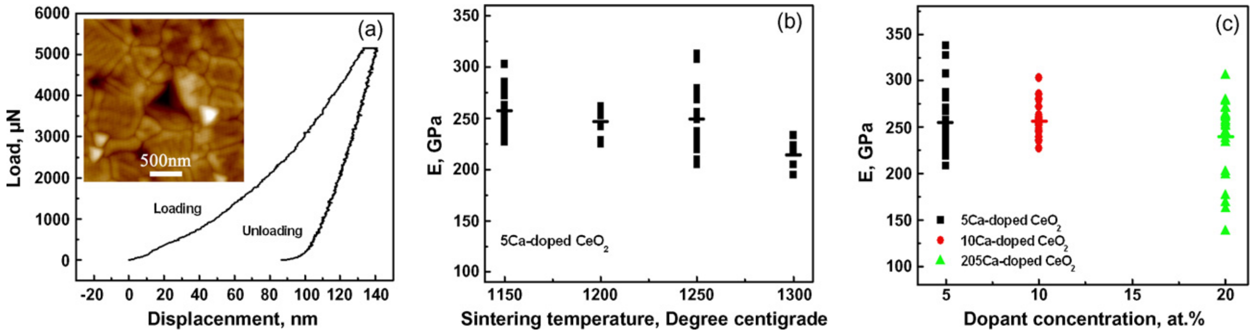

Fig. 7. (a) A typical load–unload curve from the nanoindentation test on 20Ca-1150. The inset shows the AFM image of the indentation, (b) elastic modulus for 5Ca-doped CeO_2 as a function of the sintering temperature, and (c) elastic modulus for Ca-doped CeO_2 as a function of the dopant concentration. Short lines in (b) and (c) denote the average values of the data points.

table, Ca-doped CeO_2 appears to be a tougher material than RE-doped CeO_2, showing a higher fracture toughness when the doping amount is within the solution limit (less than 20%). Beyond this, however, CaO will be formed in the system, which negatively affects the toughness since CaO itself is a much less tough material (K_{IC}, ~0.75 MPa $m^{1/2}$).[37] In fact, these revealed properties make the currently developed Ca-doped CeO_2 even comparable to a commercialized electrolyte material, 8 at.% Y_2O_3-stabilized ZrO_2, which normally shows a fracture toughness around 2.71 MPa $m^{1/2}$.[17] By way of adding trace elements or adopting rapid sintering techniques,[16,38,39] it is possible to further improve the mechanical performance of Ca-doped CeO_2, enhancing its chance as a cost-effective electrolyte material for SOFCs.

4. Conclusions

The following conclusions can be made on the differently sintered $Ce_{1-x}Ca_xO_{2-y}$ ($x = 0.05$, 0.1 and 0.2):

(1) It is found that multiple Ca-doped CeO_2 phases may exist in the seemingly one single Ca-doped CeO_2 system; this multiple-phase coexisting phenomenon may be also realizable for other doped CeO_2 materials that with large lattice deviations resulted from the element doping.

(2) The chemical state of the Ce element is less dependent on the sintering temperature, while increasing the sintering temperature may cause segregation of the Ca element in the outside layers of the sintered Ca-doped CeO_2.

(3) Ca-doped CeO_2 demonstrates a high elastic modulus around 250 GPa and a high fracture toughness around 3.4 MPa $m^{1/2}$, showing a better fracture resistance when compared to RE-doped CeO_2. Its hardness and elastic modulus decrease slightly with the increasing sintering temperature.

References

1. Haile, S. M., *Acta Mater.*, 2003, **51**, 5981.
2. Zhang, Y. H., Huang, X. Q., Lu, Z., Liu, Z. G., Ge, X. D., Xu, J. H., Xin, X. S., Sha, X. Q. and Su, W. H., *J. Alloys. Compd.*, 2007, **428**, 302.
3. Huang, X. Q., Liu, Z. G., Lu, Z., Pei, L., Zhu, R. B., Liu, Y. Q., Miao, J. P., Zhang, Z. G. and Su, W. H., *J. Phys. Chem. Solids*, 2003, **64**, 2379.
4. Mogensen, M., Sammes, N. M. and Tompsett, G. A., *Solid State Ionics*, 2000, **129**, 63.
5. Huang, X. Q., Lu, Z., Pei, L., Liu, Z. G., Liu, Y. Q., Zhu, R. B., Miao, J. P., Zhang, Z. G. and Su, W. H., *J. Alloys. Compd.*, 2003, **360**, 294.
6. Zhao, L. J., Huang, X. Q., Zhu, R. B., Lu, Z., Sun, W. W., Zhang, Y. H., Ge, X. D., Liu, Z. G. and Su, W. H., *J. Phys. Chem. Solids*, 2008, **69**, 2019.
7. Herle, J. V., Horita, T., Kawada, T., Sakai, N., Yokokawa, H. and Dokiya, M., *J. Eur. Ceram. Soc.*, 1996, **16**, 961.
8. Zhang, Y. H., Huang, X. Q., Lu, Z., Liu, Z. G., Ge, X. D., Xu, J. H., Xin, X. S., Sha, X. Q. and Su, W. H., *J. Power Sources*, 2006, **160**, 1217.
9. Zhu, B., Liu, X. R., Sun, M. T., Ji, S. J. and Sun, J. C., *Solid State Sci.*, 2003, **5**, 1127.
10. Lu, Z., Huang, X. Q., Liu, W., He, T. M., Liu, Z. G., Liu, J. and Su, W. H., *J. Rare Earths*, 2002, **20**, 47.
11. Mori, T., Buchanan, R., Ou, D. R., Ye, F., Kobayashi, T., Kim, J. D., Zou, J. and Drennan, J., *J. Solid State Electrochem.*, 2008, **12**, 841.
12. Mori, T., Wang, Y. R., Drennan, J., Auchtolonie, G., Li, J. G. and Ikegami, T., *Solid State Ionics*, 2004, **175**, 641.
13. Borchert, H., Borchert, Y., Kaichev, V. V., Prosvirin, I. P., Alikina, G. M., Lukashevich, A. I., Zaikovskii, V. I., Moroz, E. M., Paukashtis, E. A., Bukhtiyarov, V. I. and Sadykov, V. A., *J. Phys. Chem. B*, 2005, **109**, 20077.
14. Sato, K., Yugami, H. and Hashida, T., *J. Mater. Sci.*, 2004, **39**, 5765.
15. Wang, Y. L., Duncan, K., Wachsman, E. D. and Ebrahimi, F., *Solid State Ionics*, 2007, **178**, 53.
16. Zhang, T. S., Zeng, Z. Q., Huang, H. T., Hing, P. and Kilner, J., *Mater. Lett.*, 2002, **57**, 124.
17. Dudek, M., Bogusz, W., Zych, L. and Trybalska, B., *Solid State Ionics*, 2008, **179**, 164.
18. Shemilt, J. E., Williams, H. M., Edirisinghe, M. J., Evans, J. R. G. and Ralph, B., *Scripta Mater.*, 1997, **36**, 929.
19. Ma, J., Zhang, T. S., Kong, L. B., Hing, P., Leng, Y. J. and Chan, S. H., *J. Eur. Ceram. Soc.*, 2004, **24**, 2641.

[20]. Yan, M., Mori, T., Zou, J. and Drennan, J., *J. Am. Ceram. Soc.*, 2009., doi:10.1111/j.1551-2916.2009.03284.x.

21. Yan, M., Mori, T., Ye, F., Ou, D. R., Zou, J. and Drennan, J., *J. Eur. Ceram. Soc.*, 2008, **28**, 2709.
22. Matsui, T., Kosaka, T., Inaba, M., Mineshige, A. and Ogumi, Z., *Solid State Ionics*, 2005, **176**, 663.
23. Oliver, W. C. and Pharr, G. M., *J. Mater. Res.*, 1992, **7**, 1564.
24. Cook, R. F., Lawn, B. R. and Fairbank, C. J., *J. Am. Ceram. Soc.*, 1985, **68**, 604.
25. Anstis, G. R., Chantikul, P., Lawn, B. R. and Marshall, D. B., *J. Am. Ceram. Soc.*, 1981, **64**, 533.
26. Yan, M., Mori, T., Zou, J., Ye, F., Ou, D. R. and Drennan, J., *Acta Mater.*, 2009, **57**, 722.
27. Arai, H., Kunisaki, T., Shimizu, Y. and Seiyama, T., *Solid State Ionics*, 1986, **20**, 241.
28. Blumenthal, R. N., Brugner, F. S. and Garnier, J. E., *J. Electrochem. Soc.*, 1973, **120**, 1230.
29. Huang, W., Shuk, P. and Greenblatt, M., *Chem. Mater.*, 1997, **9**, 2240.
30. Eguchi, K., Setoguchi, T., Inoue, T. and Arai, H., *Solid State Ionics*, 1992, **52**, 165.
31. Crist, B. V., *Handbook of Monochromatic XPS Spectra in the Elements and Native Oxides*. John Wiley & Sons, 2000.
32. Hoang, M., Hughes, A. E. and Turney, T. W., *Appl. Surf. Sci.*, 1993, **72**, 55.
33. Paparazzo, E., *J. Vac. Sci. Technol. A*, 2004, **22**, 2188.
34. Zhang, T. S., Ma, J., Huang, H. T., Hing, P., Xia, Z. T., Cha, S. H. and Kilner, J. A., *Solid State Sci.*, 2003, **5**, 1505.
35. Chourashiya, M. G., Patil, J. Y., Pawer, S. H. and Jadhav, L. D., *Mater. Chem. Phys.*, 2008, **109**, 39.
36. Balazs, G. B. and Glass, R. S., *Solid Sate Ionics*, 1995, **76**, 155.
37. Maiya, P. S., Russell, R., Poa, D. S., Wagh, A. S. and Poeppel, R. B., *J. Mater. Res.*, 1993, **8**, 1387.
38. Fe, Y. P., Tseng, C. W. and Peng, P. C., *J. Eur. Ceram. Soc.*, 2008, **28**, 85.
39. Takeuchi, T., Kondoh, I., Tamari, N., Balakrishnan, N., Nomura, K., Kageyama, H. and Takeda, Y., *J. Electrochem. Soc.*, 2002, **149**, A455.